Catalysis Science & Technology

Accepted Manuscript

This article can be cited before page numbers have been issued, to do this please use: J. Zhou and L. D. Chen, *Catal. Sci. Technol.*, 2026, DOI: 10.1039/D6CY00510A.

ROYAL SOCIETY OF CHEMISTRY

rsc.li/catalysis

View Article Online
DOI: 10.1039/D6CY00510A

Journal Name

ARTICLE TYPE

Cite this: DOI: 00.0000/xxxxxxxxxx

Theoretical Insights into Designing β-M@Ni(OH)$_2$ Electrocatalysts for Efficient Urea Oxidation

Jingwen Zhou[a] and Leanne D. Chen*[a]

Received Date
Accepted Date

DOI: 00.0000/xxxxxxxxxx

Ni-based catalysts show great potential for the urea oxidation reaction (UOR) due to their high activity, low cost, and broad energy and environmental applications. Herein, we investigate two possible mechanisms for N_2 formation on β-Ni(OH)$_2$ using density functional theory (DFT) and further focus on the dehydrogenation steps of the intramolecular pathway over β-Ni(OH)$_2$ and β-M@Ni(OH)$_2$ catalysts (M = Cr, Fe, Co, Cu, Mo, Ru, Rh, Pd, Ir, Pt, and Au). The results show that the intramolecular pathway is energetically favourable on β-Ni(OH)$_2$, and that the enhanced urea adsorption energy, E_{ads}(urea), over β-M@Ni(OH)$_2$ is closely associated with the upshift of the d-band centre, ε_d, induced by M-doping. Gibbs free energy analyses identify β-Fe@Ni(OH)$_2$, β-Co@Ni(OH)$_2$, and β-Pd@Ni(OH)$_2$ as promising catalysts with low limiting potentials. Furthermore, the urea adsorption strength shows a linear correlation with the calculated limiting potentials, suggesting that it can serve as an effective descriptor for urea oxidation toward N_2 formation. This study provides theoretical guidance for the screening and design of highly active Ni-based UOR catalysts.

1 Introduction

The electrochemical urea oxidation reaction (UOR) is regarded as a cost-efficient and environmentally sustainable strategy in terms of environmental protection and energy storage and conversion.[1–3] For example, UOR shows great potential in urea-rich wastewater treatment as well as in direct urea fuel cells.[4,5] Moreover, as an anodic reaction, UOR represents an attractive alternative to the oxygen evolution reaction (OER) in hydrogen generation due to its substantially lower theoretical potential (1.23 V and 0.066 V vs. RHE for OER and UOR, respectively).[6] However, UOR involves a complicated six proton-coupled electron transfer steps in the reaction, which limits its efficiency and overall performance.[2,7] Therefore, effective electrocatalysts are usually required to reduce overpotential and accelerate the reaction kinetics.[3,8–10]

The exploration of UOR catalysts in recent years have increasingly focused on Ni-based materials, including bimetallic (e.g., NiFe,[11–14] NiCo,[15–18] NiCu,[19,20] NiPt,[21,22] NiPd,[23,24] and NiRh[25–27]) and trimetallic systems (e.g., Ni-Pt-Ir,[28] PtPdNi/C,[29] and $Mn_{0.5}Ni_{2.0}Fe_{0.5}$/rGO[30] due to their remarkable catalytic performance and long-term durability.[31] Moreover, the surface of Ni-based catalysts can be gradually oxidized to higher-valence Ni species, such as NiO, Ni(OH)$_2$, and NiOOH, under alkaline conditions.[10] These reconstructed Ni-based surfaces, particularly Ni(OH)$_2$-derived structures, are widely considered as the active sites for UOR.[7,31,32] To further enhance the catalytic activity, doping Ni with a secondary metal has emerged as an effective strategy. For example, Wang et al. experimentally and computationally investigated the effect of Co doping on the AOR performance of Ni(OH)$_2$.[33] The optimized 5% Co–Ni(OH)$_2$ exhibited the highest catalytic activity (1.357 V vs RHE at 100 mA cm^{-2}) and excellent stability (over 100 h at 10 mA cm^{-2}). This improvement was attributed to the Co dopant, which modulated the electronic structure of Ni(OH)$_2$ via an inductive effect, leading to a reduced Ni^{2+}/Ni^{3+} redox potential and facilitating the formation of active NiOOH species. These experimental observations were further supported by DFT calculations, showing that the d-band centre of Co-NiOOH is upshifted relative to NiOOH, which strengthens the adsorption of reaction intermediates and promotes the reaction. Pd incorporation has also been shown to enhance catalyst stability by reducing the strong adsorption of CO_2 on Ni(OH)$_2$. For example, Mathew et al. employed a facile two-step room-temperature method to synthesize Pd/Ni(OH)$_2$ catalysts.[34] Electrochemical analysis revealed maximum current densities of 180 mA cm^{-2} and 380 mA cm^{-2} for Ni(OH)$_2$ and Pd/Ni(OH)$_2$, respectively.

Although introducing a second transition metal into Ni-based catalysts has led to noticeable improvements in UOR performance, extensive experimental studies have demonstrated that multiple factors, including the reaction environment,[35–37] catalyst surface structure,[38,39] and electronic structure modulation induced by metal doping,[40] can significantly influence N_2 selec-

[a] Electrochemical Technology Centre, Department of Chemistry, University of Guelph, Guelph, Ontario N1G 2W1, Canada.
* E-mail: leanne.chen@uoguelph.ca.

View Article Online
DOI: 10.1039/D6CY00510A

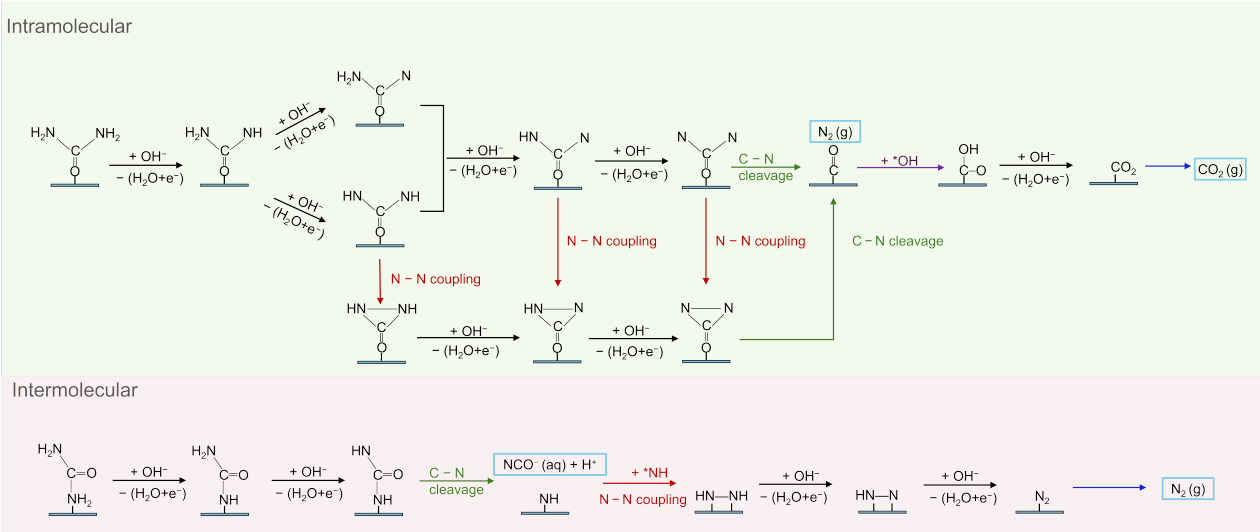

Fig. 1 Representative mechanisms for N_2 formation in the UOR.

tivity and activity, leading to increased complexity in reaction mechanisms and pathway selection. Therefore, further theoretical studies should clarify key mechanistic aspects, including the identification of active sites, the role of key intermediates in governing reaction activity, and the pathways responsible for N−N coupling. In addition, current studies mainly focus on doping 3*d* transition metals,[14,16,20,41–44] while the development of effective descriptors in theoretical works is crucial for the large-scale screening and evaluation of high-performance Ni-based catalysts. In this work, β-Ni(OH)$_2$ was selected as the parent structure for UOR reaction because it provides a well-defined structure for systematically investigating the UOR process.[45] Compared with other oxidized Ni-based surfaces, which may involve more complex surface environments and variable O/OH surface states under electrochemical conditions.[46] M@Ni(OH)$_2$ was constructed by doping representative 3*d*, 4*d*, and 5*d* transition metals onto the Ni(OH)$_2$ surface, where M = Cr, Fe, Co, Cu, Mo, Ru, Rh, Pd, Ir, Pt, and Au to examine and compare their UOR performance and reaction mechanisms.

2 Computational methods

2.1 Structures

We adopted the optimized bulk β-Ni(OH)$_2$ (mp-27912) structure from our group's previous work,[47] which was selected from the Materials Project and is consistent with experimental results. A (2×2×4) β-Ni(OH)$_2$ slab model was constructed, in which the top two layers were fully relaxed, the bottom two layers were fixed, and a 16 Å vacuum region was introduced along the *z* direction between adjacent images. In addition, a surface Ni atom was substituted by an M atom to generate β-M@Ni(OH)$_2$ (M = Cr, Fe, Co, Cu, Mo, Ru, Rh, Pd, Ir, Pt, and Au), with a surface dopant concentration of 25%.

2.2 Calculation Settings

All calculations were performed using spin-polarized periodic density functional theory (DFT) as implemented in the Vienna ab initio Simulation Package (VASP),[48,49] in combination with the Atomic Simulation Environment (ASE) interface.[50] The projector augmented-wave (PAW) pseudopotentials[51,52] were used to describe the core–valence interactions with an energy cutoff of 500 eV. Van der Waals interactions between the adsorbates and alloy surfaces were accounted for using the DFT-D3 dispersion correction.[53] Moreover, a 4×4×1 (8×8×1) Monkhorst–Pack *k*-point mesh[54] was used for geometry optimization (density of states calculations). Geometry optimizations were performed until the total energy and atomic forces converged to below 10^{-5} eV and 0.05 eV Å^{-1}, respectively. The generalized gradient approximation with a Hubbard *U* correction (GGA+*U*) was applied to selected metals, the values are listed in Table 1.[47,55] The Gibbs free energies (ΔG) of the elementary steps involved in the UOR were calculated using a previously reported CHE model:[56]

Table 1 Hubbard *U* parameters for different metal atoms.

Metal	Hubbard *U* (eV)
Ni	5.50
Cr	2.25
Fe	4.00
Co	3.72
Cu	6.75
Ir	2.00

$$\Delta G = \Delta E + \Delta E_{ZPE} + \int_0^T \Delta C_p \, dT - T\Delta S - eU \quad (1)$$

where ΔE is the reaction energy obtained from DFT calculations, $\int_0^T \Delta C_p dT$ accounts for the thermal contribution to enthalpy, *T* denotes the absolute temperature, *U* represents the applied electrode potential, *e* is the elementary charge, and ΔS denotes the entropy change. The effect of pH = 14 was also considered in this work to be consistent with experimental conditions.[57] Adsorption free energies were referenced to a clean surface and urea(g),

View Article Online
DOI: 10.1039/D6CY00510A

H_2(g), as well as H_2O(l). The equilibrium potentials (U_{eq}) for the N_2 formation via intramolecular and intermolecular mechanism were taken as $U_{eq} = -0.76$ V versus RHE and $U_{eq} = -0.55$ V versus RHE, respectively.[58] Moreover, the definition of the *d*-band centre (ε_d) is obtained as the average energy of the entire *d*-band[59]:

$$\varepsilon_d = \frac{\int_{-\infty}^{\infty} \varepsilon \rho(\varepsilon) \mathrm{d}\varepsilon}{\int_{-\infty}^{\infty} \rho(\varepsilon) \mathrm{d}\varepsilon} \quad (2)$$

where ε and $\rho(\varepsilon)$ refer to the energy of the orbital states and the density of states (DOS) at energy ε, respectively.[60] ε_d values for all calculations were extracted from the calculated results using the analysis tool VASPKIT.[61]

3 Results and Discussion

3.1 Mechanism on Pristine Ni(OH)$_2$

The generally accepted mechanisms for N_2 formation in UOR on the Ni-based catalyst can be classified into two categories, intramolecular and intermolecular,[4] as show in Fig. 1. In the intramolecular mechanism, one turnover of the reaction involves only one urea molecule.[62] Specifically, urea undergoes successive dehydrogenation to form the $^*CON_2$ intermediate, accompanied by intramolecular N–N coupling. The subsequent cleavage of the C–N bond in $^*CON_2$ generates N_2(g) and *CO, with *CO being further oxidized to CO_2. In the intermolecular mechanism, N–N coupling involves nitrogen species derived from two different urea molecules.[58] Urea undergoes dehydrogenation to form the $^*CO(NH)_2$ intermediate, followed by C–N bond cleavage to generate NCO^- (aq) and *NH species. The resulting *NH then couples with another *NH and is further dehydrogenated to N_2.

We first calculated the free energy diagrams for urea ($CO(NH_2)_2$) oxidation to N_2 formation based on two mechanisms. For the intramolecular mechanism, the initial adsorption configuration of urea involves the O atom binding to surface Ni atoms at a hollow site, and the adsorption energy E_{ads}(urea) is −0.84 eV. In addition, during the first four dehydrogenation steps of the intramolecular mechanism, the second dehydrogenation step, namely the asymmetric depronation from $^*OCNHNH_2$ to $^*OCNNH_2$, requires a lower free energy than the symmetric formation of *OCNHNH, due to the stronger adsorption of $^*OCNNH_2$ (Fig. 2(a)). The corresponding energy difference is 0.29 eV. The further deprotonation of $^*OCNNH_2$ is identified as the potential-determining step (PDS) in the intramolecular mechanism, with a free energy of 1.31 eV. Notably, the N–N bond gradually forms during this step, with the bond length decreasing from 2.373 Å in $^*OCNNH_2$ to 1.733 Å in *OCNNH. All remaining steps after the first four dehydrogenation steps are exergonic except for CO_2 desorption. The limiting potential (U_{lim}) of the intramolecular pathway is 0.55 V. Accordingly, reducing the free energy of $^*OCNNH_2$ deprotonation is the key to enhancing the overall reaction activity on β-Ni(OH)$_2$ in the intramolecular mechanism.

For the intermolecular mechanism, the N atom of urea points toward the surface. The configuration after the first dehydrogenation step, $^*NHCONH_2$, is distinct from the intramolecular case, where the N atom serves as the adsorption site and favours subsequent intermolecular N–N coupling.[4] This adsorption energy of urea is −0.52 eV. The free energy diagram indicates that the symmetric dehydrogenation of $^*NHCONH_2$ to *NHCONH is the PDS along the intermolecular pathway, and the corresponding free energy is 1.34 eV, as shown in Fig. 2(b). In addition, the subsequent C–N bond cleavage of *NHCONH is thermodynamically unfavourable. This step remains energetically uphill even at the limiting potential ($U_{lim} = 0.79$ V for the intermolecular pathway), because it is a non-electrochemical step. Comparing the free energy profiles of the two mechanisms, the PDS for both pathways are located within the first four dehydrogenation steps, and the intramolecular mechanism for urea oxidation toward N_2 is energetically preferred over the intermolecular mechanism. These results are in agreement with previous studies that also identified early-stage dehydrogenation as the energetically critical process and the intramolecular pathway as the preferred mechanism for UOR on Ni-based hydroxide catalysts.[34,40,58,63] Therefore, in this work, we employed calculations of the first four steps in the intramolecular mechanism as an efficient strategy to screen high-performance UOR β-M@Ni(OH)$_2$ catalysts.

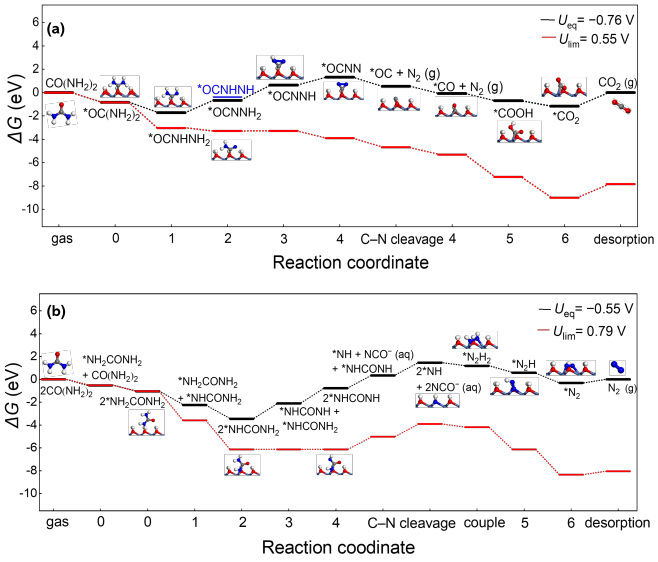

Fig. 2 Gibbs energy diagrams for the intramolecular (a) and intermolecular (b) pathways over pristine β-Ni(OH)$_2$.

3.2 *d*-band Centre Analysis

The adsorption configurations of urea on β-Ni(OH)$_2$ and β-M@Ni(OH)$_2$ are classified into three groups according to the adsorption sites, as shown in Fig. 3. The configuration of Fe@Ni(OH)$_2$, Co@Ni(OH)$_2$, Cu@Ni(OH)$_2$, Rh@Ni(OH)$_2$, and Pd@Ni(OH)$_2$ is consistent with that on pristine Ni(OH)$_2$, where the O atom preferentially occupies a threefold hollow site (Ni_1–Ni_2–M). The remaining configurations adopt bridge-site geometries with different coordinating atoms, for example, configurations of Cr@Ni(OH)$_2$, Mo@Ni(OH)$_2$, and Ru@Ni(OH)$_2$ adsorb at the M–Ni_2 bridge site, whereas configurations of Ir@Ni(OH)$_2$, Pt@Ni(OH)$_2$, and Au@Ni(OH)$_2$ occupy the bridge site formed by

View Article Online
DOI: 10.1039/D6CY00510A

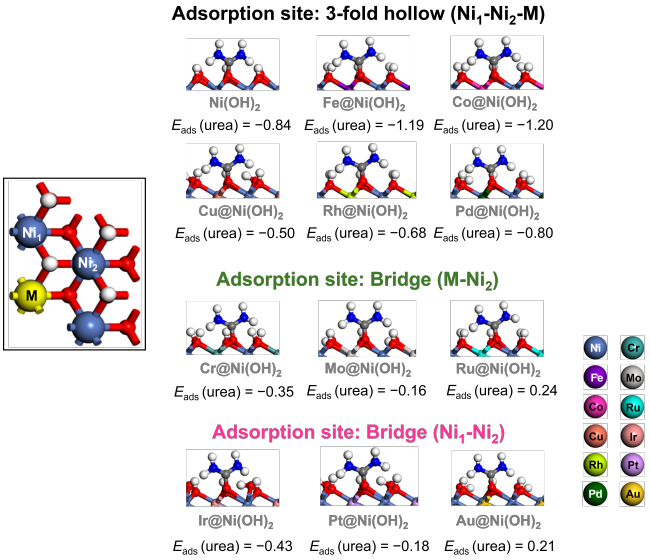

Fig. 3 Optimized urea adsorption configurations and adsorption energies E_{ads}(urea) in eV over the β-Ni(OH)$_2$ and β-M@Ni(OH)$_2$ surfaces. The inset shows the various adsorption sites.

two Ni atoms, the Ni_1–Ni_2 site. The bond lengths between the oxygen atom of urea and surface metal atoms (Ni or M) are summarized in Table 2. The calculated E_{ads}(urea) indicate that adsorption at the bridge sites is generally weaker than the threefold hollow site.

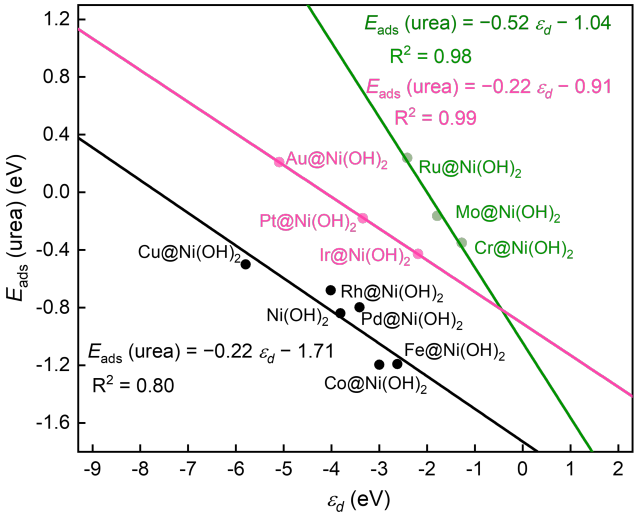

Fig. 4 Correlation between adsorption energy of urea, E_{ads}(urea), and the d-band centre, ε_d, grouped by the most favoured adsorption site pristine β-Ni(OH)$_2$ and β-M@Ni(OH)$_2$.

We further calculated the d-band centre (ε_d) of β-Ni(OH)$_2$ and β-M@Ni(OH)$_2$, where the surface atoms were selected according to the most favourable urea adsorption sites. Linear relationships between the ε_d and E_{ads}(urea) were observed for each adsorption-site group, as shown in Fig. 4. These results suggest that the variation in urea adsorption strength upon M-doping correlates with the shift of the d-band centre toward the Fermi level,

Table 2 Adsorption site, O–metal (Ni/M) bond lengths of adsorbed urea in Å, and bond length differences $|\Delta l|$ on β-Ni(OH)$_2$ and β-M@Ni(OH)$_2$.

Dopant	Adsorption Site	O–Ni_1	O–Ni_2	O–M	$\|\Delta l\|$
Pristine	Ni_1–Ni_2–M	2.36	2.25	2.26	0.11
Fe	Ni_1–Ni_2–M	2.32	2.20	2.31	0.12
Co	Ni_1–Ni_2–M	2.32	2.21	2.26	0.11
Cu	Ni_1–Ni_2–M	2.26	2.20	2.31	0.11
Rh	Ni_1–Ni_2–M	2.41	2.24	2.34	0.17
Pd	Ni_1–Ni_2–M	2.29	2.18	2.31	0.13
Cr	M–Ni_2	2.52	2.16	2.15	0.37
Mo	M–Ni_2	2.50	2.20	2.19	0.31
Ru	M–Ni_2	2.58	2.15	2.14	0.44
Ir	Ni_1–Ni_2	2.13	2.22	2.72	0.59
Pt	Ni_1–Ni_2	2.30	2.22	2.61	0.39
Au	Ni_1–Ni_2	2.16	2.21	2.69	0.53

suggesting that an upshift of the d-band centre generally favors stronger urea adsorption. Although adsorption configuration and local structural effects may also contribute to the adsorption behavior, the modulation of the d-band centre still provides a useful electronic explanation for understanding the observed adsorption trends within the present systems.

3.3 Comparison of Pristine Ni(OH)$_2$ and M@Ni(OH)$_2$

Fig. 5 systematically compares the dehydrogenation pathways on β-Ni(OH)$_2$ and β-M@Ni(OH)$_2$. The order of dehydrogenation steps on these M-doped catalysts is divided into two different classes. For example, Co@β-Ni(OH)$_2$, similar to pristine β-Ni(OH)$_2$, favours asymmetric dehydrogenation from *OCNHNH$_2$ to form *OCNNH$_2$, whereas the remaining β-M@Ni(OH)$_2$ surfaces prefer symmetric dehydrogenation from *OCNHNH$_2$ to generate *OCNHNH. In addition, doping with M atoms can alter the PDS and its free energy on specific β-M@Ni(OH)$_2$ surfaces. Based on their PDS, the surfaces were divided into three groups. (1) When the PDS is the second dehydrogenation step, i.e., dehydrogenation of *OCNHNH$_2$, the surfaces are β-Fe@Ni(OH)$_2$, β-Cu@Ni(OH)$_2$, β-Pd@Ni(OH)$_2$, β-Ir@Ni(OH)$_2$, and β-Pt@Ni(OH)$_2$. (2) When the PDS is the third dehydrogenation step, for pristine β-Ni(OH)$_2$ this corresponds to dehydrogenation of *OCNNH$_2$, and for β-Ru@Ni(OH)$_2$ and β-Au@Ni(OH)$_2$ this corresponds to dehydrogenation of *OCNHNH. (3) Lastly, when PDS is the last dehydrogenation step, i.e., the dehydrogenation of *OCNNH, the surfaces are β-Cr@Ni(OH)$_2$, β-Co@Ni(OH)$_2$, β-Mo@Ni(OH)$_2$, and β-Rh@Ni(OH)$_2$. The free energies of these PDS follow the order of 1.08 eV < 1.18 eV < 1.27 eV < 1.31 eV < 1.34 eV < 1.38 eV < 1.41 eV < 1.56 eV < 1.57 eV ≈ 1.57 eV < 1.67 eV < 2.04 eV on the β-Co@Ni(OH)$_2$, β-Fe@Ni(OH)$_2$, β-Pd@Ni(OH)$_2$, β-Ni(OH)$_2$, β-Rh@Ni(OH)$_2$, β-Cu@Ni(OH)$_2$, β-Pt@Ni(OH)$_2$, β-Cr@Ni(OH)$_2$, β-Ir@Ni(OH)$_2$,

View Article Online
DOI: 10.1039/D6CY00510A

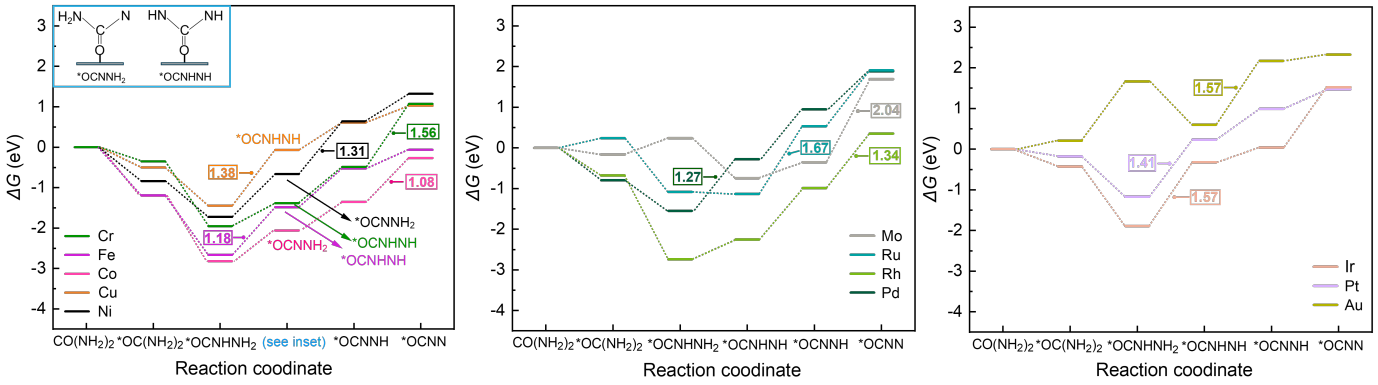

Fig. 5 Gibbs energy diagrams for the dehydrogenation steps of the intramolecular pathway on β-Ni(OH)$_2$ and β-M@Ni(OH)$_2$ catalyst doped with (a) 3*d*, (b) 4*d*, and (c) 5*d* M transition metals (M = Cr, Fe, Co, Cu, Mo, Ru, Rh, Pd, Ir, Pt, and Au). The number inside the rectangle represents the free energy of the potential-determining step for each catalyst.

β-Au@Ni(OH)$_2$, β-Ru@Ni(OH)$_2$, and β-Mo@Ni(OH)$_2$ surfaces, respectively. These calculated free energies show that β-Co@Ni(OH)$_2$, β-Fe@Ni(OH)$_2$, and β-Pd@Ni(OH)$_2$ are promising high-performance UOR catalyst candidates, the results are in agreement with previous experimental studies,[33,34,40,63] suggesting that doping Co, Fe, and Pd on β-Ni(OH)$_2$ is an effective strategy to enhance the activity of Ni-based catalysts. The calculated U_{lim} for each catalyst is shown in Table 3. The configurations of the first four dehydrogenation steps on β-Ni(OH)$_2$ and β-M@Ni(OH)$_2$ are denoted in Fig. S1. The N–N bond length decreases toward bond formation during the dehydrogenation from *OCNNH$_2$ (or *OCNHNH) to *OCNN, except for β-Mo@Ni(OH)$_2$, β-Ru@Ni(OH)$_2$, β-Rh@Ni(OH)$_2$, and β-Ir@Ni(OH)$_2$. It is worth noting that *OCNN binds to the β-Mo@Ni(OH)$_2$ surface via the N atom rather than the O atom, unlike the adsorption configuration on other catalyst surfaces. We will discuss the outlying behaviour of β-Mo@Ni(OH)$_2$ in the following section.

Table 3 Limiting potentials (U_{lim}) of the PDS for UOR over β-Ni(OH)$_2$ and β-M@Ni(OH)$_2$.

Catalyst	U_{lim} (V)
Ni(OH)$_2$	0.55
Cr@Ni(OH)$_2$	0.80
Fe@Ni(OH)$_2$	0.42
Co@Ni(OH)$_2$	0.32
Cu@Ni(OH)$_2$	0.62
Mo@Ni(OH)$_2$	1.28
Ru@Ni(OH)$_2$	0.91
Rh@Ni(OH)$_2$	0.58
Pd@Ni(OH)$_2$	0.51
Ir@Ni(OH)$_2$	0.81
Pt@Ni(OH)$_2$	0.65
Au@Ni(OH)$_2$	0.81

3.4 E_{ads} (urea) as Activity Descriptor

The establishment of effective descriptors is generally regarded as an efficient bridge linking key adsorbates with catalytic activity, enabling the efficient screening and prediction of high-performance electrocatalysts.[64–66] Here, we observe a linear relationship between E_{ads}(urea) and U_{lim}, i.e., stronger urea adsorption leads to a lower U_{lim} on β-Ni(OH)$_2$ and β-M@Ni(OH)$_2$ (Fig. 6), indicating that high-performance Ni-based UOR catalysts can be achieved by tuning the E_{ads}(urea). A similar trend is also observed on the β-NiOOH surface.[46] It should be noted that excessively strong E_{ads}(urea) may over-stabilize surface intermediates, which may increase the free energy required for subsequent dehydrogenation steps. In practical catalyst design, the balance between adsorption strength and subsequent reaction activity should be further considered, although a detailed investigation of this aspect is beyond the scope of this work.

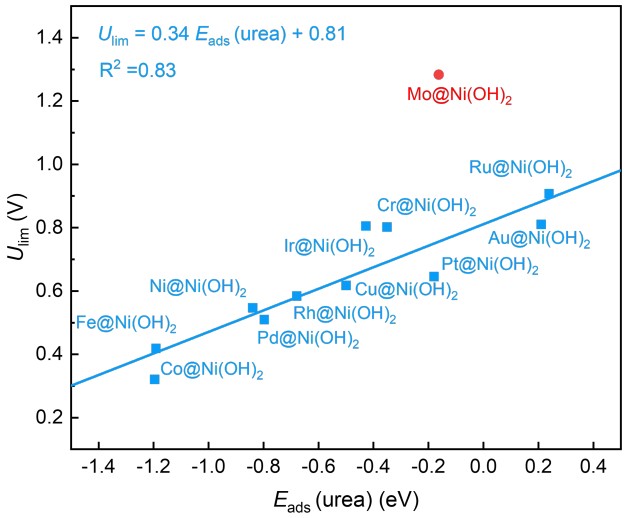

Fig. 6 Linear correlations of E_{ads} (urea) and U_{lim} on the Ni(OH)$_2$ and M@Ni(OH)$_2$.

Notably, the β-Mo@Ni(OH)$_2$ still follows the overall trend be-

View Article Online
DOI: 10.1039/D6CY00510A

tween E_{ads} (urea) and U_{lim}. However, it appears as an outlier from the linear scaling relationship. This deviation originates from the adsorption configuration in the potential-determining step. On the other β-M@Ni(OH)$_2$ catalyst surfaces, the *OCNN intermediate generally maintains a stable O–bound adsorption configuration. However, on β-Mo@Ni(OH)$_2$, the high oxophilicity of the Mo dopant leads to an overly strong Mo−O interaction during geometry optimization. This strong interaction competes with the intrinsic O−C bonding within the *OCNN intermediate, leading to cleavage of the O−C bond and destabilization of the original intermediate structure. In contrast, when adopting an N–bound adsorption configuration, such as *NCON on β-Mo@Ni(OH)$_2$, the intermediate structure can remain intact because the direct strong interaction between O and Mo is avoided (see Fig. S1 in the Supplementary Information). However, the rearrangement of the adsorption structure from an O−bound to an N−bound configuration on β-Mo@Ni(OH)$_2$ considerably increases the free energy of the potential-determining step. In addition, combined with the relationship between ε_d and E_{ads} (urea) discussed above, we find that the improved catalytic performance induced by M-atom doping can be rationalized by the modulation of ε_d. Therefore, the E_{ads} (urea) serves as an effective descriptor for screening and predicting potential UOR electrocatalysts. We propose that catalysts with adsorption energies of urea around or below −0.84 eV, which is the value on β-Ni(OH)$_2$, including β-Co@Ni(OH)$_2$, β-Fe@Ni(OH)$_2$, and β-Pd@Ni(OH)$_2$, can be promising Ni-based catalysts.

Conclusion

In this work, we conducted a systematic investigation of the UOR mechanism and catalytic performance on β-Ni(OH)$_2$ and β-M@Ni(OH)$_2$ surfaces, where M = Cr, Fe, Co, Cu, Mo, Ru, Rh, Pd, Ir, Pt, and Au. The main conclusions are summarized in the following.

1. The free energy diagrams show that the intramolecular pathway is energetically more favourable than the intermolecular pathway on all β-Ni(OH)$_2$ surfaces. Moreover, the dehydrogenation steps in both mechanisms are identified as the PDS, specifically the dehydrogenation of *OCNNH$_2$ in the intramolecular pathway and the dehydrogenation of *NHCONH$_2$ in the intermolecular pathway.

2. The modulation of the *d*-band centre induced by M-atom doping plays an important role in the changes of urea adsorption energies on β-Ni(OH)$_2$ and β-M@Ni(OH)$_2$ surfaces.

3. The calculated free energy diagram for the four dehydrogenation steps shows that M-doping can effectively lower the free energy of the PDS and thus the limiting potential. Based on our results, we propose that β-Co@Ni(OH)$_2$, β-Fe@Ni(OH)$_2$, and β-Pd@Ni(OH)$_2$ are promising Ni-based UOR catalyst candidates.

4. The adsorption energy of urea is an effective descriptor for AOR activity. An upshift of the *d*-band centre generally strengthens the adsorption of urea, which contributes to a reduction in the limiting potential and thus improve catalytic activity. Catalysts with E_{ads}(urea) around or below −0.84 eV, the value on β-Ni(OH)$_2$, can be considered improved Ni-based catalysts for UOR.

Author Contributions

J. Zhou: conceptualization, data curation, formal analysis, validation, visualization, writing – original draft, writing – review & editing. L. D. Chen: conceptualization, funding acquisition, project administration, resources, supervision, writing – review & editing.

Conflicts of interest

There are no conflicts to declare.

Data availability

The data supporting this article have been included as part of the Supplementary Information.

Acknowledgements

The authors gratefully acknowledge the Natural Sciences and Engineering Research Council of Canada (Discovery Grant, RGPIN-2020-07095) for financial support of this work. All DFT calculations are enabled by Advanced Research Computing resources generously provided by the Digital Research Alliance of Canada (RRG-5307).

References

1 A. K. Satheesan, R. Madhu, S. Nagappan, H. N. Dhandapani, A. De, S. S. Roy, P. Mazumder and S. Kundu, *Chemical Communications*, 2025.
2 J. Gautam, S.-Y. Lee and S.-J. Park, *Advanced Energy Materials*, 2025, **15**, 2406047.
3 J. Wang, M. Sun, X. Zhang, J. Liu, J. He, W. Ge, S. Kong, G. Zhang, M. Gao, Z. Sun *et al.*, *Advanced Materials*, 2025, e15043.
4 X. Gao, S. Zhang, P. Wang, M. Jaroniec, Y. Zheng and S.-Z. Qiao, *Chemical Society Reviews*, 2024, **53**, 1552–1591.
5 G. Gnana kumar, A. Farithkhan and A. Manthiram, *Advanced Energy and Sustainability Research*, 2020, **1**, 2000015.
6 J. J. Medvedev, N. H. Delva and A. Klinkova, *ChemPlusChem*, 2024, **89**, e202300739.
7 Y. Zeng, S. Xiang, S. Lu and X. Qi, *Materials*, 2024, **17**, 2617.
8 S. Xu, X. Ruan, M. Ganesan, J. Wu, S. K. Ravi and X. Cui, *Advanced Functional Materials*, 2024, **34**, 2313309.
9 A. S. Rasal, H. M. Chen and W.-Y. Yu, *Nano Energy*, 2024, **121**, 109183.
10 F. Guo, D. Cheng, Q. Chen, H. Liu, Z. Wu, N. Han, B.-J. Ni and Z. Chen, *Progress in Natural Science: Materials International*, 2024, **34**, 362–375.
11 A. Modak, R. Mohan, K. Rajavelu, R. Cahan, T. Bendikov and A. Schechter, *ACS Applied Materials & Interfaces*, 2021, **13**, 8461–8473.

View Article Online
DOI: 10.1039/D6CY00510A

12 S. C. Dhawale, A. V. Munde, B. B. Mulik, R. P. Dighole, S. S. Zade and B. R. Sathe, *Langmuir*, 2024, **40**, 2672–2685.
13 X. Yin, K. Zhu, K. Ye, J. Yan, D. Cao, D. Zhang, J. Yao and G. Wang, *Journal of Colloid and Interface Science*, 2024, **654**, 36–45.
14 Y. Diao, Y. Liu, G. Hu, Y. Zhao, Y. Qian, H. Wang, Y. Shi and Z. Li, *Biosensors and Bioelectronics*, 2022, **211**, 114380.
15 B. Feng, W. Jiang, R. Deng, J. Lu, P. Tsiakaras and S. Yin, *Journal of Colloid and Interface Science*, 2024, **663**, 1019–1027.
16 X. Gao, Y. Wang, W. Li, F. Li, H. Arandiyan, H. Sun and Y. Chen, *Electrochimica Acta*, 2018, **283**, 1277–1283.
17 W. Xu, H. Zhang, G. Li and Z. Wu, *Scientific reports*, 2014, **4**, 5863.
18 W. Yan, D. Wang and G. G. Botte, *Electrochimica Acta*, 2012, **61**, 25–30.
19 M. Wala, A. Blacha-Grzechnik, A. Stolarczyk, S. Bajkacz, P. Dydo and W. Simka, *International Journal of Hydrogen Energy*, 2023, **48**, 34229–34243.
20 A. Abutaleb, *Catalysts*, 2019, **9**, 397.
21 D. Kutyła, M. Fukumoto, H. Takahashi, R. Takahashi, K. Skibińska and P. Żabiński, *Materials*, 2025, **18**, 5069.
22 J. R. Barbosa, C. H. Paranhos, O. C. Alves, N. R. Checca, J. P. Serna, A. L. Rossi and J. C. M. Silva, *Electrochimica Acta*, 2020, **355**, 136752.
23 A. Rodríguez-Buenrostro, A. Martínez-Lázaro, M. Contreras-Martínez, A. Sharma, G. L. Barcenas, G. Oza, A. Arenillas, J. Ledesma-García and L. Arriaga, *Materials for Renewable and Sustainable Energy*, 2024, **13**, 255–264.
24 N. Muthuchamy, S. Jang, J. C. Park, S. Park and K. H. Park, *ACS Sustainable Chemistry & Engineering*, 2019, **7**, 15526–15536.
25 P. Mirzaei, S. Bastide, A. Dassy, R. Bensimon, J. Bourgon, A. Aghajani, C. Zlotea, D. Muller-Bouvet and C. Cachet-Vivier, *Electrochimica Acta*, 2019, **297**, 715–724.
26 S. Qian, Z. Rao, Y. Liu, J. Yan, B. Fan, Y. Gui and F. Guo, *Electrochimica Acta*, 2020, **330**, 135211.
27 A. T. Miller, B. L. Hassler and G. G. Botte, *Journal of Applied Electrochemistry*, 2012, **42**, 925–934.
28 K. Hiraide, Y. Liu, K. Akiyoshi, S. Kuwabata and T. Torimoto, Electrochemical Society Meeting Abstracts prime2024, 2024, pp. 3827–3827.
29 M. Pérez-Sosa, E. Ramírez-Meneses, A. Manzo-Robledo, J. Mateos-Santiago, M. Hernández-Pérez, V. Garibay-Febles, L. Lartundo-Rojas and G. Zacahua-Tlacuatl, *International Journal of Hydrogen Energy*, 2021, **46**, 21419–21432.
30 P. Basumatary, U. H. Lee, D. Konwar and Y. S. Yoon, *International Journal of Hydrogen Energy*, 2020, **45**, 32770–32779.
31 C. Zhang, S. Chen, L. Guo, Z. Li, C. Yan and C. Lv, *Chinese Journal of Chemistry*, 2024, **42**, 3441–3468.
32 X. Gao, J. Dong, H. Yang, C. Ni, X. He, Z. Li and L. Tian, *Journal of Alloys and Compounds*, 2025, 178477.
33 Y. Wang, Y. Lu, Y. Shi, J. Wang, Y. Zheng, J. Pan, C. Li and J. Cao, *Applied Surface Science*, 2023, **640**, 158391.
34 N. Mathew, R. Rathod, S. Saha, P. K. Santra, S. K. Pati and M. Eswaramoorthy, *Chemistry–An Asian Journal*, 2025, **20**, e202401188.
35 C. Fan, M. Zhang, Y. Li, Y. Zhang, Y.-Q. Wang, F. Gong and J. Liu, *Nature Communications*, 2026.
36 W. Jiang, J. Zhang, J. Wu, Z. Zhai, T. Yu, L. Luo and S. Yin, *Advanced Energy Materials*, 2026, **16**, e03978.
37 W. Jiang, Z. Zhai, X. Zhuo, J. Wu, B. Feng, T. Yu, H. Wen and S. Yin, *Chinese Journal of Structural Chemistry*, 2025, **44**, 100519.
38 S. W. Tatarchuk, J. J. Medvedev, F. Li, Y. Tobolovskaya and A. Klinkova, *Angewandte Chemie International Edition*, 2022, **61**, e202209839.
39 J. Li, J. Li, T. Liu, L. Chen, Y. Li, H. Wang, X. Chen, M. Gong, Z.-P. Liu and X. Yang, *Angewandte Chemie*, 2021, **133**, 26860–26866.
40 L. Chen, W. Jiang, J. Zhang, B. Chu, Z. Zhai, T. Yu, H. He and S. Yin, *ACS Sustainable Chemistry & Engineering*, 2024, **12**, 10466–10474.
41 Z. Zhao, Y. Zhou, T. Kang, X. Wu, S. Jin, M. Yuan and X. Chang, *Inorganic Chemistry*, 2026.
42 Z. Ji, S. Zhao, Z. Wang, L. Hao, J. Li, F. Cheng, M. Hussain, W. Su and J. Liu, *Journal of Power Sources*, 2026, **674**, 239796.
43 C. Xie, C. Zhou, Y. Zhang, B. Zhou, Y. Yao, B. Li, J. Li, J. Bai, M. Long, K. Jiang *et al.*, *Angewandte Chemie International Edition*, 2026, e25119.
44 W. Jiang, X. Zhuo, T. Yu, J. Lu, Z. Zhai, H. Wen and S. Yin, *ACS Sustainable Chemistry & Engineering*, 2024, **12**, 998–1006.
45 D. S. Hall, D. J. Lockwood, C. Bock and B. R. MacDougall, *Proceedings of the Royal Society A: Mathematical, Physical and Engineering Sciences*, 2015, **471**, 20140792.
46 Q. Jin, M. X. Garcia-Ortiz and L. Árnadóttir, *Journal of Catalysis*, 2025, 116503.
47 S. J. Johnston, R. M. Choueiri, X. Liu, B. J. Laframboise, S. W. Tatarchuk and L. D. Chen, *The Journal of Physical Chemistry C*, 2024, **128**, 5568–5578.
48 G. Kresse and J. Hafner, *Physical review B*, 1993, **47**, 558.
49 G. Kresse and J. Furthmüller, *Physical review B*, 1996, **54**, 11169.
50 A. H. Larsen, J. J. Mortensen, J. Blomqvist, I. E. Castelli, R. Christensen, M. Dułak, J. Friis, M. N. Groves, B. Hammer, C. Hargus *et al.*, *Journal of Physics: Condensed Matter*, 2017, **29**, 273002.
51 P. E. Blöchl, *Physical review B*, 1994, **50**, 17953.
52 G. Kresse and D. Joubert, *Physical review b*, 1999, **59**, 1758.
53 S. Grimme, J. Antony, S. Ehrlich and H. Krieg, *The Journal of chemical physics*, 2010, **132**, 154104.
54 H. J. Monkhorst and J. D. Pack, *Physical review B*, 1976, **13**, 5188.
55 J. Liu, J. Xiao, Z. Wang, H. Yuan, Z. Lu, B. Luo, E. Tian and G. I. Waterhouse, *ACS Catalysis*, 2021, **11**, 5386–5395.
56 J. K. Nørskov, J. Rossmeisl, A. Logadottir, L. Lindqvist, J. R. Kitchin, T. Bligaard and H. Jonsson, *The Journal of Physical Chemistry B*, 2004, **108**, 17886–17892.

View Article Online
DOI: 10.1039/D6CY00510A

57 R. K. Singh and A. Schechter, *Electrochimica Acta*, 2018, **278**, 405–411.
58 S. W. Tatarchuk, R. M. Choueiri, A. J. MacKay, S. J. Johnston, W. M. Cooper, K. S. Snyder, J. J. Medvedev, A. Klinkova and L. D. Chen, *ChemPhysChem*, 2024, **25**, e202300889.
59 N. J. K., S. Felix, Abild-Pedersen and B. thomas, *Fundamental Concepts in Heterogeneous Catalysis*, John Wiley & Sons, 2014.
60 B. J. Laframboise, J. Coveny, J. Zhou and L. D. Chen, *ChemElectroChem*, 2025, **12**, e202500288.
61 V. Wang, N. Xu, J.-C. Liu, G. Tang and W.-T. Geng, *Computer Physics Communications*, 2021, **267**, 108033.
62 W. Chen, L. Xu, X. Zhu, Y.-C. Huang, W. Zhou, D. Wang, Y. Zhou, S. Du, Q. Li, C. Xie *et al.*, *Angewandte Chemie International Edition*, 2021, **60**, 7297–7307.
63 Z. Zheng, D. Wu, L. Chen, S. Chen, H. Wan, G. Chen, N. Zhang, X. Liu and R. Ma, *Applied Catalysis B: Environmental*, 2024, **340**, 123214.
64 J. Zhou, J. S. Chung and S. G. Kang, *The Journal of Physical Chemistry C*, 2024, **129**, 303–313.
65 R. K. Sharma, H. Minhas and B. Pathak, *The Journal of Physical Chemistry Letters*, 2026.
66 J. Zhou, J. S. Chung and S. G. Kang, *International Journal of Hydrogen Energy*, 2024, **58**, 745–752.

View Article Online
DOI: 10.1039/D6CY00510A

The data supporting this article have been included as part of the Supplementary Information.